The nebular emission of star-forming galaxies in a hierarchical universe

Álvaro Orsi[1,2]⋆, Nelson Padilla [1,2], Brent Groves [3], Sofía Cora [4,5,6], Tomás Tecce [1,2], Ignacio Gargiulo [4] and Andrés Ruiz [6,7,8]

1. Instituto de Astrofísica, Pontificia Universidad Católica, Av. Vicuña Mackenna 4860, Santiago, Chile.
2. Centro de Astro-Ingeniería, Pontificia Universidad Católica, Av. Vicuña Mackenna 4860, Santiago, Chile.
3. Max Planck Institute for Astronomy, Königstuhl 17 D-69117 Heidelberg, Germany
4. Instituto de Astrofísica de La Plata (CCT La Plata, CONICET, UNLP), Paseo del Bosque s/n, B1900FWA, La Plata, Argentina.
5. Facultad de Ciencias Astronómicas y Geofísicas, Universidad Nacional de La Plata, Paseo del Bosque s/n, B1900FWA, La Plata, Argentina.
6. Consejo Nacional de Investigaciones Científicas y Técnicas, Rivadavia 1917, C1033AAJ Buenos Aires, Argentina.
7. Instituto de Astronomía Teórica y Experimental (CCT Córdoba, CONICET, UNC), Laprida 854, X5000BGR, Córdoba, Argentina.
8. Observatorio Astronómico de Córdoba, Universidad Nacional de Córdoba, Laprida 854, X5000BGR, Córdoba, Argentina.

24 February 2014

ABSTRACT
Galaxy surveys targeting emission lines are characterising the evolution of star-forming galaxies, but there is still little theoretical progress in modelling their physical properties. We predict nebular emission from star-forming galaxies within a cosmological galaxy formation model. Emission lines are computed by combining the semi-analytical model `SAG` with the photo-ionization code `MAPPINGS-III`. We characterise the interstellar medium (ISM) of galaxies by relating the ionization parameter of gas in galaxies to their cold gas metallicity. Our model is in reasonable agreement with the observed Hα, [OII]$\lambda 3727$ and [OIII]$\lambda 5007$ luminosity functions. Also, the model reproduces the star-forming sequence of the BPT diagram for local galaxies and the observed Hα to [OII]$\lambda 3727$ line ratios at high redshift. The average ionization parameter predicted for galaxies is found to increase in galaxies with low star-formation rates and also towards higher redshifts, in agreement with recent observational results. We study the relation between the star-formation rate of galaxies and their emission line luminosities as a function of redshift, finding strong correlations between different emission lines and their star-formation rates. We present scaling relations that can be used to infer the star-formation rate using only single line luminosities. Our model predicts that high redshift emission line galaxies have modest clustering bias, and thus reside in by dark matter haloes of masses below $M_{\mathrm{halo}} \lesssim 10^{12}[\mathrm{h}^{-1}\mathrm{M}_\odot]$, consistent with observational estimates of the clustering of emission lines. We present predictions for the number of star-forming galaxies that can be detected at redshifts up to $z \sim 10$ by targeting different far-infrared (FIR) emission lines with submillimetre facilities such as the Atacama Large Millimeter Array (ALMA). Finally, we discuss the limitations of our modelling technique and the possible ways to extend it.

Key words: galaxies:high-redshift – galaxies:evolution – methods:numerical

1 INTRODUCTION

Emission lines are a common feature in the spectra of galaxies. A number of physical processes occurring in the interstellar medium (ISM) of galaxies can be responsible for their production, such as the recombination of ionized gas, collisional excitation or fluorescent excitation (Osterbrock 1989; Stasińska 2007). Their detection allows the exploration of the physical properties of the medium from which they are produced. Active galactic nuclei (AGN), for instance, can photoionise and shock-heat the gas in the narrow-line region surrounding the accretion disks of supermassive black holes (Groves, Dopita & Sutherland 2004a,b). Also, cold gas falling into the galaxy's potential well might radiate its energy away via collisional excitation (Dijkstra & Loeb 2009).

Likewise, star-forming activity in galaxies can be traced by the detection of emission lines (Kennicutt 1983; Calzetti 2012). Young, massive stars produce photo-ionizing radiation which is absorbed by the neutral gas of the ISM leading to the production of emission

⋆ Email: aaorsi@astro.puc.cl

lines. Given the short life-times of massive stars (of the order of a few Myr), emission lines indicate the occurrence of recent episodes of star formation. On the contrary, continuum-based tracers of star forming (SF) activity, such as the UV continuum, are tracing the star formation rate (SFR) over a much larger time-scale of the order of ~ 100 Myr. Regardless of the technique used, mapping the cosmic evolution of star formation to understand the formation and evolution of galaxies has become an important challenge in extragalactic astrophysics (Madau, Pozzetti & Dickinson 1998; Hopkins 2004).

The link between emission line fluxes and the properties of the gas in the ISM have naturally made their detection a common tool in extragalactic astrophysics. Theoretical modelling of emission lines has focused mostly in providing a tool to learn about the dynamics and structure of the gas in galaxies. Typically, the interpretation of line fluxes and line ratios is done by making use of a photo-ionization radiative transfer code (Ferland et al. 1998; Dopita et al. 2000; Kewley et al. 2001). Line ratios and fluxes can then be translated into gas metallicities, temperatures, densities and the ionizing structure of the gas (e.g. Kewley & Ellison 2008; Levesque, Kewley & Larson 2010). By using a number of ad-hoc assumptions, it is also possible to include nebular emission into a stellar population synthesis code (Charlot & Longhetti 2001; Panuzzo et al. 2003). Individual objects can be studied in great detail when both optical and infrared emission lines are available, constraining the properties of the multi-phase ISM and the contribution of each ISM component to the total emission line budget (e.g. Abel et al. 2005; Cormier et al. 2012).

Analysis of the emission line budget has also been done in large galaxy datasets. In the local spectroscopic sample of galaxies from the Sloan Digital Sky Survey (SDSS), Tremonti et al. (2004) made use of several line ratios finding a global relation between the gas metallicity and the stellar mass of galaxies. The exact shape and normalization of this relation is somewhat controversial, since metallicity diagnostics using different line ratios can lead to different values of metallicity (Kewley & Ellison 2008; Cullen et al. 2013). Despite the uncertainty in the exact value of the gas metallicity inferred by measuring line ratios, it is clear that the mass-metallicity relation encodes information about the evolution of the chemical enrichment of galaxies, which in turn depends on the formation history of galaxies, their stellar mass growth, the feedback mechanisms controlling the star-formation processes, and the merging histories of galaxies.

The narrow-band technique to find emission lines in high redshift galaxies has been extensively applied to large samples at different redshifts. The HiZELS survey (Geach et al. 2008) has produced a sample of high redshift star-forming galaxies large enough to measure the luminosity function and clustering of Hα and [OII]$\lambda 3727$ emitters over the redshift range $0.4 < z < 2.2$ (Sobral et al. 2010; Geach et al. 2012; Hayashi et al. 2013; Sobral et al. 2013). More recently, using slitless grism spectroscopy from the Hubble Space Telescope, the PEARS survey sampled a large number of Hα, [OII]$\lambda 3727$ and [OIII]$\lambda 5007$ emission line galaxies (ELGs) over the redshift range $0 < z < 1.5$ (Xia et al. 2011; Pirzkal et al. 2013).

At high redshifts, hydrogen recombination and forbidden lines are also targeted to derive galaxy redshifts and also physical properties, such as the star-formation rate (SFR) and the gas metallicitiy (e.g. Nagao, Maiolino & Marconi 2006; Maier et al. 2006). Galaxies at high redshifts have been found to have lower gas metallicities for a given stellar mass compared to their $z = 0$ counterparts, thus suggesting an evolution of the mass-metallicity relation (Erb

et al. 2006; Maiolino et al. 2008; Yuan, Kewley & Richard 2013). More recently, a fundamental relation between gas metallicity, stellar mass and star-formation rate has been suggested (Mannucci et al. 2010; Lara-López et al. 2010) which seems to hold independent of redshift (see, however, Troncoso et al. 2013).

From a cosmological perspective, the search for the most distant galaxies is key to understand the sources that reionised the Universe (Meiksin 2009; Bunker et al. 2010; Raičević, Theuns & Lacey 2011). Searching for the Lyman break is a common technique to select galaxy candidates for these extreme high redshift galaxies. Normally, spectroscopic confirmation of their redshift is needed, which consists in detecting a strong emission line, such as Lyα (e.g. Pentericci et al. 2007; Stark et al. 2010; Schenker et al. 2011). Emission lines are also targeted in large area surveys to measure the large scale structure of the Universe at high redshifts. Cosmological probes such as the detection of baryonic acoustic oscillations (BAOs) and the growth rate of cosmic structures at different redshifts are powerful tests that could revolutionize our cosmological paradigm. Ambitious programs have been proposed, including space missions such as EUCLID, whose goal is to detect $\sim 10^8$ Hα emitters in the redshift range $0.5 < z < 2.2$, (Laureijs et al. 2010), ground-based programs such as HETDEX (Hill et al. 2008; Blanc et al. 2011), which expects to detect $\sim 10^6$ Lyα emitters over the redshift range $2.5 < z < 3.5$, and multi narrow-band wide field surveys such as PAU and J-PAS which have also the potential to study the large scale structure of the Universe traced by emission line galaxies (Abramo et al. 2012).

However, despite the significant observational progress which has increased the depth and area in surveys of ELGs, little theoretical work has been made aiming at understanding the emission line galaxy population as a whole. Emission from the ^{12}CO molecule has been studied by Lagos et al. (2012) in a galaxy formation model, where the molecular gas content is key to predict the luminosity from different rotational transitions of ^{12}CO. Also, a number of studies have focused in the Lyα line, which, unlike the lines generated by the ^{12}CO molecule, is originated in HII regions (e.g. Le Delliou et al. 2006; Dayal, Ferrara & Saro 2010; Kobayashi, Totani & Nagashima 2010; Orsi, Lacey & Baugh 2012). The intrinsic production of Lyα photons from recombination of photo-ionized hydrogen is not a challenge to the models, but the high Lyα cross section of scattering with hydrogen atoms results in the path lengths of photons being large enough to make them easily absorbed by even small amounts of dust. Predictions for Lyα emitters were presented in detail in Orsi, Lacey & Baugh (2012) including the escape of Lyα photons through galactic outflows computed with a Monte Carlo radiative transfer model.

In this work we extend the modelling of ELGs by focusing in other nebular emission lines in the optical and far-infrared (FIR) range. The ELG population is studied by making use of a fully fledged semi-analytical model of galaxy formation. The SAG model (acronym for Semi-Analytic galaxies; Cora 2006; Lagos, Cora & Padilla 2008) makes use of N-body dark matter simulations to follow the abundances and merging history of dark matter haloes where astrophysical processes shape the formation and evolution of galaxies. Predictions of Hα emission in star-forming galaxies were presented in Orsi et al. (2010) making use of the semi-analytical model GALFORM. Here we extend the range of predictions by combining the SAG model with the photo-ionizing code MAPPINGS-III (Dopita et al. 2000; Levesque, Kewley & Larson 2010) to predict the luminosities of forbidden lines in the optical such as [OII]$\lambda 3727$ and [OIII]$\lambda 5007$ and far-infrared (FIR) lines such as [NII]$\lambda 205 \mu$m.

The paper is organized as follows: Section (2) briefly de-

scribes the semi-analytical model `SAG` and the photo-ionization code `MAPPINGS-III` that we use in this work. Section (3) presents our strategy to compute the emission lines of galaxies. Section (4) shows how our predictions compare to observational measurements and describes predictions of the properties of ELGs. In Section (5) we present predictions for very high redshift galaxies that could be observed with submillimetre facilities. Then, in Section (6) we discuss the validity of our modelling strategy. Finally, in Section (7) we summarize and present the main conclusions of this work.

2 THE MODELS

We compute nebular emission from star-forming activity in galaxies by combining two different models. The semi-analytical model of galaxy formation `SAG` is the backbone of this work. This model predicts the physical and observational properties of a large number of galaxies at virtually any redshift. The predicted galaxy properties are combined with the `MAPPINGS-III` photoionization code to predict emission line luminosities due to star-forming activity. In the following, we give a brief description of both models and our strategy to obtain the nebular emission of star forming galaxies.

2.1 The galaxy formation model

`SAG` is a semi-analytical model in which the formation and evolution of galaxies is followed based on a hierarchical structure formation cosmology. In short, the model determines the heating and radiative cooling of gas inside dark matter haloes, the formation of stars from cold gas, the feedback mechanisms from supernova explosions and AGN activity regulating the star formation process, the formation of the bulge component during bursts of star-formation associated to galaxy mergers or disk instabilities, the chemical enrichment of the ISM of galaxies and the spectral evolution of the stellar components.

In this work, we make use of the latest variant of `SAG` presented in Gargiulo et al. (2014). We refer the reader looking for a full description of the `SAG` model to Cora (2006); Lagos, Cora & Padilla (2008); Tecce et al. (2010); Ruiz et al. (2013) and Gargiulo et al. (2014). In the following, we describe the features of `SAG` that are more relevant to this work.

The backbone of the `SAG` model are merger trees of dark matter subhaloes taken from a N-body simulation. This simulation is based on the standard ΛCDM scenario, characterized by the cosmological parameters $\Omega_{\rm m} = 0.28$, $\Omega_{\rm b} = 0.046$, $\Omega_\Lambda = 0.72$, $h = 0.7$, $n = 0.96$, $\sigma_8 = 0.82$, according to the WMAP7 cosmology (Jarosik et al. 2011). The simulation was run using GADGET-2 (Springel 2005) using 640^3 particles in a cubic box of comoving sidelength $L = 150 h^{-1}$Mpc. In a postprocessing step of the outputs of the simulation, the formation, evolution, merging histories and internal structure of dark matter haloes and subhaloes are computed by using a 'friends-of-friends' and then the SUBFIND algorithms (Springel et al. 2001).

We have introduced a calculation of the spectral energy distribution (SED) of each model galaxy as a result of their individual star formation history, based on the stellar population synthesis code Charlot & Bruzual 2007, an updated version of the Bruzual & Charlot (2003) code. Unlike previous versions of `SAG` where photometric data was available for only a handful of filters at the rest-frame, the detailed calculation of the SED of galaxies allows us to obtain magnitudes from any filter and the continuum flux around

the emission lines we are interested, which is used to compute the equivalent width (EW) of emission lines.

Early versions of `SAG` assumed that during a starburst episode all the cold gas available is converted into stars instantaneously. This crude approximation has a dramatic impact on the ionization photon budget coming from galactic bulges, since ionizing photons only trace SF episodes over the last ~ 10 Myr. Hence, an instantaneous SF episode creates an unrealistic old population of bulge stars, with few or no ionizing photons.

In the latest variant of `SAG`, Gargiulo et al. (2014) introduced an extended SF period for starbursts, in which these are characterized by a certain time-scale in which the cold gas is gradually consumed. The cold gas that will be eventually converted in bulge stars is referred to as bulge cold gas, in order to differentiate it from the disk cold gas. The time-scale for consuming the bulge cold gas is chosen to be the dynamical time-scale of the disk. However, as the starburst progresses, effects of supernovae feedback, recycling of gas from dying stars and black hole growth modify the reservoir of cold gas of both disk and bulge, thus also changing the time-scale of the starburst, as shown in Gargiulo et al. (2014).

The `SAG` model contains a number of free parameters. To find an optimal set of parameter values we use the Particle Swarm Optimization technique described in Ruiz et al. (2013). The multidimensional space defined by the free parameters is explored in order to localize the minimum that reproduces a set of observables, including the local optical luminosity functions, the black hole mass to bulge mass relation and supernovae rates up to $z \sim 1.5$.

For simplicity, in this work we assume that stars are formed following a universal Initial Mass Function (IMF) given by Salpeter (1955). The calibration of `SAG` using the observational data described above assuming a Salpeter IMF can be found in the Appendix of Gargiulo et al. (2014).

2.2 The photo-ionization code

`MAPPINGS-III` is a shock and photo-ionization code for modelling emission lines in the ISM. A detailed description of the code can be found in Dopita et al. (2000); Kewley et al. (2001) and Levesque, Kewley & Larson (2010).

`MAPPINGS-III` is a one dimensional code, which simplifies the radiation transfer, at the price of limiting the geometries that can be explored. Typically, a `MAPPINGS-III` run consists of a central point source emitting an ionizing radiation field, surrounded by a region of gas with a given density, filling factor and chemical abundance. At a given radius, within the Stromgen sphere radius, the equations of ionization and thermal equilibrium are solved in thin shells of increasing radius from the central source, making use of the *on-the-spot* approximation for the diffuse radiation, taking into account the absorption of the ionizing continuum and the geometric dilution. At the Stromgen radius, the emission-line intensities are computed integrating over the ionized volume.

We use the publicly available grid of `MAPPINGS-III` results presented in Levesque, Kewley & Larson (2010). The code features a robust calculation of hydrogenic recombination, collisional excitation and nebular continuum processes over all wavelengths. Also, a rigorous modelling of dust including absorption, charging and photoelectric heating by dust grains is included (Groves, Dopita & Sutherland 2004a). To relate the properties of the HII region and the galaxy `MAPPINGS-III` is combined with the Starburst99 code (Leitherer et al. 1999), which predicts a synthetic ionizing radiation as a function of metallicity, age and star formation history

(SFH). These quantities are used to relate the grid of ionization parameter and metallicity to observable galaxy properties.

In this work we do not use the Starburst99 spectra directly. The `SAG` model computes a composite SED based on the predicted SFH of each galaxy. Hence, the ionizing photon production rate computed by `SAG` is used as an input to obtain the emission line fluxes predicted by `MAPPINGS-III` as a function of ionization parameter q and gas metallicity Z at age zero. The `MAPPINGS-III` grid of emission line fluxes used is run for an electron density $n_e = 10 [\text{cm}^{-3}]$. Also, the grid consists of 5 gas metallicity values spanning the range $0.001 \leqslant Z \leqslant 0.04$ and 7 ionization parameter values in the range $10^7 \leqslant q[\text{cm/s}] \leqslant 4 \times 10^8$. For any given combination of q and Z we perform a bi-linear interpolation restricting the possible values of both q and Z to the range within the grid. The procedure to obtain these two values for any galaxy is described in the following section.

3   EMISSION LINE LUMINOSITIES OF SAG GALAXIES

The line fluxes predicted by `MAPPINGS-III` are conveniently characterised by two properties of the HII regions: the gas metallicity and the ionization parameter. The electron density, n_e, is taken to be a constant, $n_e = 10 [\text{cm}^{-3}]$. We call the flux of the emission line λ_j predicted by `MAPPINGS-III` as $F(\lambda_j, q, Z)$, for a given ionization parameter q and metallicity Z. Our semi-analytical model computes the properties of the cold gas from both the bulge and disk component of the galaxies, so we can track the metallicities of both components and use them as input to obtain the line fluxes from `MAPPINGS-III`. The local ionization parameter q is simply defined as

$$q = \frac{S_{H^0}}{n} \ [\text{s}^{-1}\text{cm}], \qquad (1)$$

where S_{H^0} is the ionizing photon flux per unit area, and n is the local number density of hydrogen atoms. Since the semi-analytical model does not resolve the internal structure of galaxies, it is not straightforward to compute these quantities.

A key quantity related to the ionization parameter is the hydrogen ionizing photon rate Q_{H^0}, defined as

$$Q_{H^0} = \int_0^{\lambda_0} \frac{\lambda L_\lambda}{hc} \mathrm{d}\lambda, \qquad (2)$$

where $\lambda_0 = 912\text{Å}$, L_λ is the composite SED of a galaxy in units of erg s^{-1} Å^{-1}, c is the velocity of light and h the Planck constant. Q_{H^0} is computed directly by `SAG` at each snapshot of the model, simply by integrating over the composite spectra predicted.

By assuming case B recombination (Osterbrock 1989) we can express the luminosity of Hα in terms of Q_{H^0} by

$$L(H\alpha) = \frac{\alpha_{H\alpha}^{\text{eff}}}{\alpha_B} h\nu_{H\alpha} Q_{H^0}, \qquad (3)$$

$$= 1.37 \times 10^{-12} Q_{H^0}, \qquad (4)$$

where $L(H\alpha)$ is in [erg s^{-1}], $\alpha_{H\alpha}^{\text{eff}}$ is the effective recombination coefficient at Hα, α_B is the case B recombination coefficient. It is expected that a fraction f_{esc} of the total ionizing photon production escapes the galaxy without contributing to the production of emission lines. In such case, Q_{H^0} is reduced by a factor $(1 - f_{\text{esc}})$ in Eq. (4). The calculation of the escape fraction of ionizing photons is a long-standing challenge in galaxy formation models. Its value is key for inferring the contribution of star-forming galaxies to the recombination of the Universe at high redshifts (Raičević,

Theuns & Lacey 2011). Deep observations searching for Lyman-continuum photons from star-forming galaxies have yielded estimated values for f_{esc} as low as zero, although in general the values derived are small and within $f_{\text{esc}} \lesssim 0.1$ (e.g. Leitherer et al. 1995; Bergvall et al. 2006; Shapley et al. 2006; Siana et al. 2007; Iwata et al. 2009). Thus, for simplicity, in this paper we assume that all ionizing photons are absorbed by the neutral medium, contributing to the nebular emission budget. This translates into the assumption of $f_{\text{esc}} = 0$.

The ionization parameter q can be estimated observationally by measuring line ratios of the same species, such as [OIII]/[OII]. It has been found that low metallicity galaxies tend to have larger values of q than galaxies with large metallicities (e.g. Maier et al. 2006; Nagao, Maiolino & Marconi 2006; Groves & Allen 2010; Shim & Chary 2013). The reason for a decrease of q with metallicity is due to both the opacity of the stellar winds, which absorb a greater fraction of ionizing photons at high metallicities, and the scattering of photons at the stellar atmospheres. Both effects reduce the ionizing flux available and thus the ionization parameter (Dopita et al. 2006a,b).

In order to mimic the resulting relation between the ionization parameter and the gas metallicity, we relate both quantities through the following power-law,

$$q(Z) = 2.8 \times 10^7 \left(\frac{Z_{\text{cold}}}{0.012} \right)^{-1.3}, \qquad (5)$$

where Z_{cold} corresponds to the metallicity of the cold gas of the disk or bulge component. The choice for the numerical values in Eq. (5) is made to find a good match when comparing between the predictions of the model with the observational data shown in the next section. For illustration, we also show in the following section model predictions obtained using fixed values of q that bracket the `MAPPINGS-III` grid, $q = 10^7$[cm/s] and $q = 4 \times 10^8$[cm/s].

Finally, $L(\lambda_j)$, the emission line luminosity of the line λ_j is computed as

$$L(\lambda_j) = 1.37 \times 10^{-12} Q_{H^0} \frac{F(\lambda_j, q, Z_{\text{cold}})}{F(H\alpha, q, Z_{\text{cold}})}. \qquad (6)$$

4   RESULTS

In this section we present several comparisons between our model predictions and observational measurements of the abundance of ELGs. To avoid an artificial incompleteness due to the limited halo mass resolution of the N-body simulation, the galaxies in `SAG` we use in our analysis are limited to having stellar masses $M_{\text{stellar}} \geqslant 10^9 [h^{-1} M_\odot]$ and Hα luminosities $L_{H\alpha} \geqslant 10^{39}$[erg s^{-1} h^{-2}].

4.1   The BPT diagram

Line ratios are a common observed property of ELGs. They are used to derive the gas metallicity and ionization parameter of both local and high redshift galaxies (Nagao, Maiolino & Marconi 2006; Kewley & Ellison 2008; Nakajima & Ouchi 2013; Guaita et al. 2013; Richardson et al. 2013), to estimate dust attenuation corrections through Balmer line decrements (Nakamura et al. 2004; Ly et al. 2007; Sobral et al. 2013), to separate star-forming from AGN activity (Kauffmann et al. 2003; Kewley et al. 2006), and also to calibrate star-formation indicators (Ly et al. 2011; Hayashi et al. 2013).

The so-called BPT diagram (Baldwin, Phillips & Ter-levich 1981) compares the line ratios [OIII]$\lambda 5007$/Hβ with
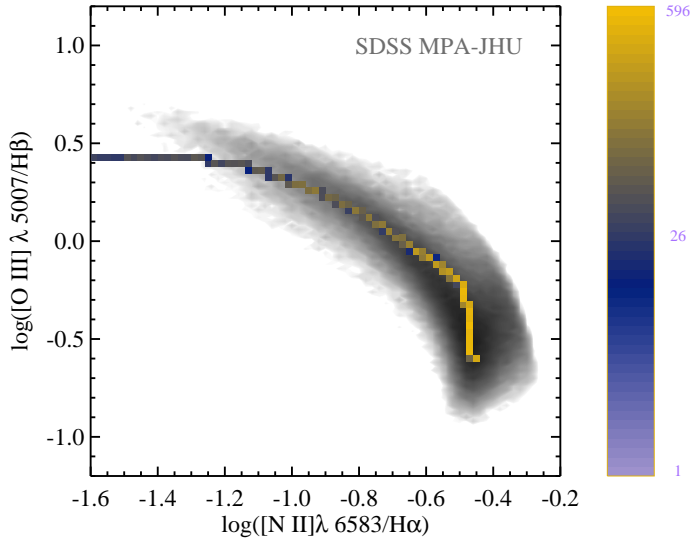
Figure 1. The BPT diagram predicted by our model (density of galaxies represented by colored shaded areas) compared with the emission line local galaxy sample from the SDSS MPA-JHU public catalogue (gray shaded region). Shown in the colour scale on the right is the number of model galaxies that correspond to each position in the BPT diagram.

Figure 2. The Hα luminosity functions predicted by our model compared to observational data at different redshifts. Model predictions are shown in blue, whereas the observational data are shown by gray symbols. The redshift of the model outputs, shown at the bottom-left side of each box, is chosen to match as closely as possible the redshift of the observations (shown in the upper-right corner of each box for each observational data set). The dashed line shows the contribution of the bulge component of galaxies to the total luminosity function.

[NII]$\lambda6584$/Hα. This line diagnostic is useful to distinguish between gas excited by SF (i.e. HII regions) versus that excited by AGN activity. Qualitatively, since hydrogen recombination lines are strongly dependent on the ionizing photon rate production Q_{H^0}, Hα and Hβ are used in the denominators of the line ratios to remove the dependence from the total ionizing photon budget, and also to minimize the effects of dust attenuation (because of the proximity of Hα $\lambda6562$ to [NII]$\lambda6584$, and Hβ $\lambda4851$ to [OIII]$\lambda5007$). Hence, both line ratios can be analyzed in terms of the ionization parameter and the metallicity of the gas. Fig.1 compares the line ratios of the BPT diagram for star-forming galaxies taken from the SDSS MPA-JHU catalogue (Kauffmann et al. 2003) with our model predictions.

When using our model for the ionization parameter q, Eq. (5), we can reproduce the shape of the BPT diagram for star forming galaxies remarkably well. This is an expected result, since we are basing our predictions for the line ratios in a photoionization model known to reproduce the BPT diagram if q is chosen to be inversely proportional to the metallicity (Dopita et al. 2006b; Kewley et al. 2013a,b). The exact form of Eq. (5) we propose here also allows us to predict a consistent luminosity function of [OII]$\lambda3727$ and [OIII]$\lambda5007$, as shown in the next section.

A change in the shape of the BPT diagram for high redshift galaxies has recently been reported (e.g. Yeh & Matzner 2012; Kewley et al. 2013a,b). This shift is probably caused by an increase of the ionization parameter of galaxies towards values that are outside the standard maximum allowed by the grid of configurations in MAPPINGS-III available to us, $q = 4 \times 10^8 [\mathrm{cm/s}]$. Our model is thus unable to reproduce such evolution of the ionization parameter, since the relation between q and Z is fixed by Eq. (5), making line ratios in galaxies at high redshift vary along the same sequence displayed by the model in Fig. 1.
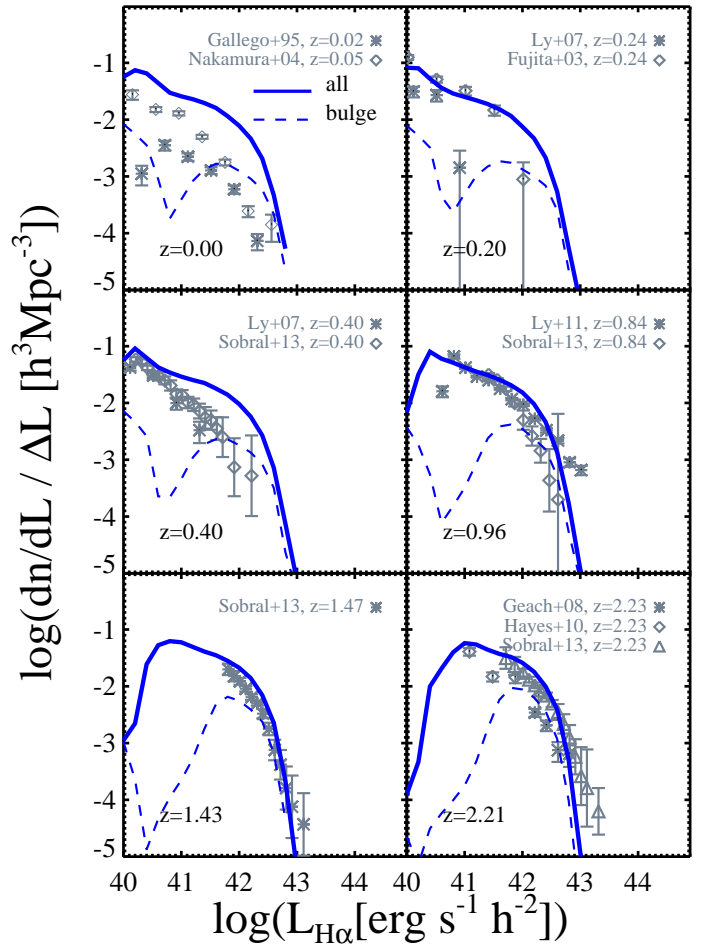
4.2 The abundance of star-forming ELGs

A basic way of characterizing a galaxy population is by measuring their luminosity function (LF) and its evolution with redshift. Here, we compare the emission-line LF predicted by our model with observational estimates at different redshifts.

The SFR over short timescales, of the order of ~ 10 Myr, is directly related with the production of ionizing photons, Q_{H^0}, which is also proportional to the Hα luminosity through Eq. (4). Hence, the Hα luminosity correlates directly with the star-formation rate of galaxies in a timescale of a few Myr. A reasonable match between the predicted and observed Hα LF as a function of redshift can thus validate the predicted cosmic evolution of star formation in the SAG semi-analytical model.

Fig. 2 shows the LF of Hα emitters at different redshifts, predicted by the models. Observational data is taken from Gallego et al. (1995); Fujita et al. (2003); Nakamura et al. (2004); Ly et al. (2007); Geach et al. (2008); Hayes, Schaerer & Östlin (2010) and Sobral et al. (2013) spanning the redshift range $0 < z < 2.2$. In order to perform a comparison with this set of observational data, we
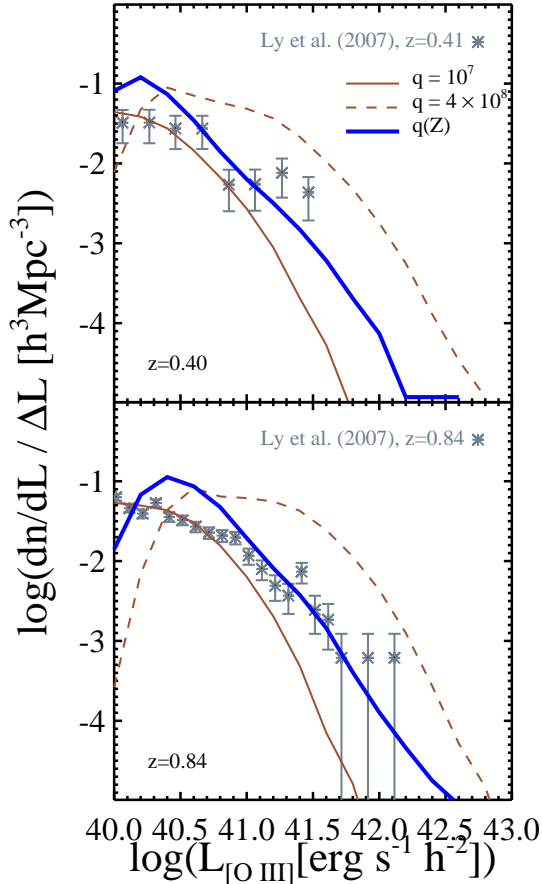
Figure 3. The [OIII]$\lambda 5007$ luminosity functions at $z \approx 0.4$ (top panel) and $z \approx 0.8$ (bottom panel). The solid blue line shows our model predictions. The solid and dashed brown lines show the results of assuming a constant value for the ionization parameter of $q = 10^7 [\mathrm{cm/s}]$ and $q = 4 \times 10^8 [\mathrm{cm/s}]$ respectively. Observational data from Ly et al. (2007) are shown with gray symbols.

selected those LFs that were corrected by dust attenuation. Also, we limit our predicted samples by an EW cut to avoid including galaxies that would not be observed due to their small EW. We compute the EW by simply taking the ratio between the line flux and the average value for the continuum within 100 Å around the wavelength of the line. We choose a rest-frame EW> 10Å, which is consistent with the typical value for the limiting EW that is used in observations.

Overall, there is a reasonable agreement between the model predictions and the observational data for $z \geqslant 0.4$. At lower redshifts, our model predicts Hα LFs that are consistent with the observed ones at the faint end, and above the observed LFs towards the bright end. At $z = 0$, our model predictions are significantly above the observed LFs of Nakamura et al. (2004) and Gallego et al. (1995).

It is worth noting that the Hα luminosity does not depend on the model for the ionization parameter. Therefore, the predicted Hα LFs shown in Fig. 2 are valid for any model of the ionization parameter.

The excess of SFR in SAG implied by the Hα luminosities at low redshift has also been studied in Ruiz et al. (2013), where the observed decline in the specific SFR from $z \sim 1$ towards $z = 0$ is shown to be steeper than what is predicted by SAG.

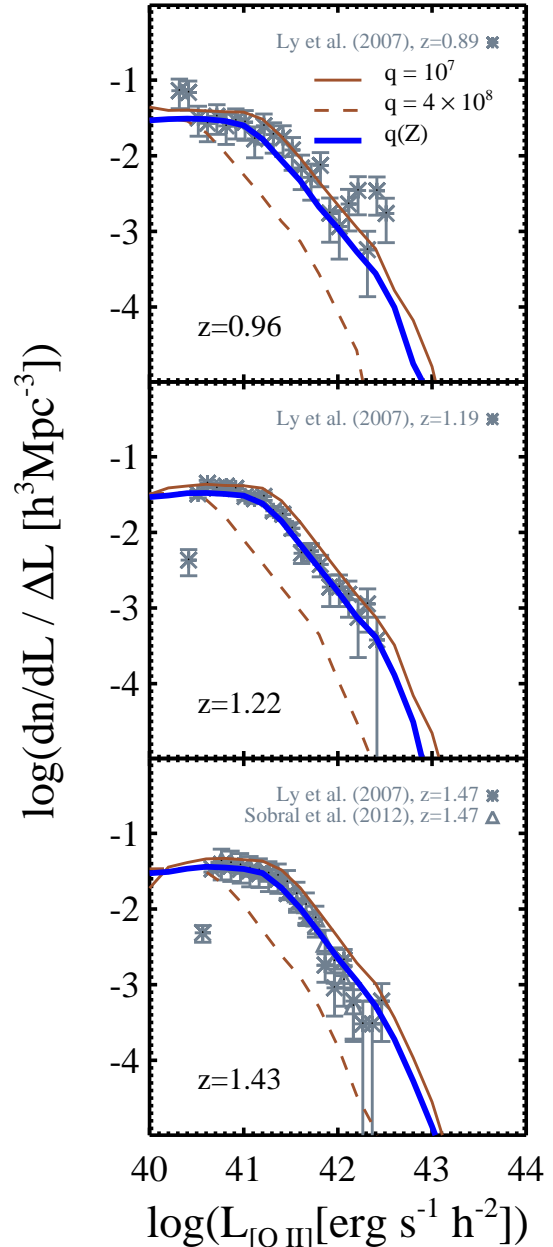The dashed lines in Fig. 2 show the contribution of star for-

Figure 4. The [OII]$\lambda 3727$ luminosity functions at $z \approx 0.96$ (top panel), $z \approx 1.2$ (mid panel) and $z \approx 1.43$ (bottom panel). The solid blue line shows our model predictions. The solid and dashed brown lines show the results of assuming a constant value for the ionization parameter of $q = 10^7 [\mathrm{cm/s}]$ and $q = 4 \times 10^8 [\mathrm{cm/s}]$ respectively. Observational data from Ly et al. (2007) and Sobral et al. (2013) are shown with gray symbols.

mation occurring in the bulge to the total luminosity function. Overall, bursty star-formation due to either merger episodes or disc instabilities contributes significantly only for Hα luminosities $L_{H\alpha} > 10^{43} [\mathrm{erg\ s^{-1}\ h^{-2}}]$ at any redshift. This means that only the brightest sources have a significant contribution of line luminosity coming from the bulge.

In order to test our choice of the model for the ionization parameter, we study the LF of forbidden lines. Fig. 3 shows the predicted [OIII]$\lambda 5007$ luminosity functions compared to observational data from Ly et al. (2007) at redshifts $z = 0.4$ and $z = 0.8$. This line luminosity, originated by collisional excitation, is sensitive to the

choice of both the ionization parameter and metallicity. For illustrating the effect of the choice of q in the LF, we plot the predictions of the model choosing a constant value of q. We adopt $q_0 = 10^7$ and $q = 4 \times 10^8 \mathrm{[cm/s]}$, since these are the lowest and highest value of q in the MAPPINGS-III grid that we use for this work. These are shown with the solid and dashed brown lines for the low and high value of q respectively.

We find an interesting trend in the predicted LFs of $[\mathrm{OIII}]\lambda 5007$, when compared to the observational data. Both predictions using a constant ionization parameter appear to enclose the observed LF of $[\mathrm{OIII}]\lambda 5007$. The model predictions with low q show a LF below the one when assuming a high value of q. The observational data seems to lie in between, somewhat favouring low values of q at bright $[\mathrm{OIII}]\lambda 5007$ luminosities. Our model predictions with q defined by Eq.(5) interpolates between these two regimes, being overall more consistent with the observational data than the models with a constant q.

The situation is reversed when looking at the $[\mathrm{OII}]\lambda 3727$ LF, as shown in Fig.4. The LF with $q = 4 \times 10^8 \mathrm{cm/s}$ is below the ones with $q = 10^7 \mathrm{cm/s}$. In this case, however, the observed LFs are slightly below the model with $q = 10^7 \mathrm{cm/s}$. Both the normalization and the slope are consistent with the model predictions at $0.9 < z < 1.4$. It is worth noticing that in this redshift range, the model $\mathrm{H}\alpha$ luminosity function is slightly above the observational measurements. Hence, it is likely that the rather good agreement between model and observations shown in Fig. 4 for the $[\mathrm{OII}]\lambda 3727$ LF is partially due to an excess of ionizing photons.

4.3 The Star-formation rate traced by emission lines

The $\mathrm{H}\alpha$ luminosity is the most common tracer of star forming activity occurring within a few Myr. Its rest-frame wavelength ($\lambda_{H\alpha} = 6562\text{Å}$) makes it accessible to optical and near-infrared facilities spanning the redshift range $0 < z < 2.2$. The inferred star-formation rate density using $\mathrm{H}\alpha$ as a function of redshift has been shown to be consistent with other star-formation estimators, such as the UV continuum (Hopkins 2004; Sobral et al. 2013). Moreover, dust extinction is usually less severe at the $\mathrm{H}\alpha$ wavelength than at shorter wavelengths. However, a variety of nebular lines are produced in HII regions and therefore these also correlate with the instantaneous star formation rate in some way. High redshift surveys that have no access to the $\mathrm{H}\alpha$ line have to rely on alternative recombination lines, such as $\mathrm{H}\beta$ (if detected) or use crude estimations based on SED fitting with a handful of photometric bands. This motivates the exploration of using non-standard forbidden lines as tracers of star-formation rate.

Fig. 5 shows our model predictions for the correlation between the $\mathrm{H}\alpha$, $[\mathrm{OII}]\lambda 3727$, $[\mathrm{OIII}]\lambda 5007$ and $[\mathrm{NII}]\lambda 205\mu\mathrm{m}$ lines with the star-formation rate at different redshifts.

Since the luminosity of a collisional excitation line depends on the ionization parameter, which in turn depends on the cold gas metallicity, in our model the relation between the line luminosities and the star formation rate evolves with redshift, reflecting the evolution of the cold gas metallicity of galaxies.

We find that it is possible to describe the relation between the star formation rate and a line luminosity, at a given redshift, by a second-order polynomial. Each term of the polynomial is found to evolve linearly with redshift, thus leading to a polynomial of the form

Table 1. Values of the constants in Eq. (7) defining the relation between the emission line luminosities and the star-formation rate. Each row corresponds to a different emission line.

Line	a	b	c	d	e	f
$\mathrm{H}\alpha$	-41.48	-	-	-	1.00	-
$[\mathrm{OII}]\lambda 3727$	298.57	-26.10	1.33	-0.01	-15.50	0.20
$[\mathrm{OIII}]\lambda 5007$	473.99	-190.35	9.29	-0.11	-24.46	0.31
$[\mathrm{NII}]\lambda 205\mu\mathrm{m}$	17.73	46.98	-2.21	0.02	-1.87	0.03

$$
\begin{aligned}
\log \dot{M}(L_\lambda, z) = & \; a + (1+z)\left[b + \log L_\lambda \left(c + d \log L_\lambda\right)\right] + \\
& \log L_\lambda \left(e + f \log L_\lambda\right),
\end{aligned} \tag{7}
$$

where $\dot{M} = \dot{M}[\mathrm{M}_\odot \mathrm{yr}^{-1}]$ is the instantaneous star-formation rate, $L_\lambda = L_\lambda [\mathrm{erg\, s^{-1}\, h^{-2}}]$ corresponds to the luminosity of the line λ, and the constants a, b, c, d, e and f are chosen by minimizing χ^2 using Eq. (7) and are different for each line. Table 1 shows the values of the constants for each line, and the dashed lines in Fig. 5 shows Eq. (7) and its evolution from $z = 5$ down to $z = 0$.

As expected, the $\mathrm{H}\alpha$ line shows a tight correlation with the SFR. In our model, there is a direct relation between the production rate of ionizing photons, Q_{H^0}, and the $\mathrm{H}\alpha$ luminosity, Eq. (4), and the latter correlates tightly with the instantaneous star-formation rate. This relation does not evolve with redshift since both the $\mathrm{H}\alpha$ luminosity and the star formation rate are related to each other through Q_{H^0} only. The ionization parameter makes no significant difference in our predictions for recombination lines.

The $[\mathrm{OII}]\lambda 3727$ luminosity correlates strongly with the SFR, although with a significant scatter. Interestingly, the scatter is reduced, from about an order of magnitude at faint luminosities of $L \sim 10^{39} [\mathrm{erg\, s^{-1} h^{-2}}]$ to virtually no scatter for $L \gtrsim 10^{42} [\mathrm{erg\, s^{-1} h^{-2}}]$.

Also, our model predicts that a fixed $[\mathrm{OII}]\lambda 3727$ luminosity corresponds to higher SFRs as we look towards higher redshifts. For instance, at $L = 10^{41} [\mathrm{erg\, s^{-1}\, h^{-2}}]$, the SFR at $z = 5$ is $\sim 1 [\mathrm{M}_\odot/\mathrm{yr}]$, and $\sim 0.1 [\mathrm{M}_\odot/\mathrm{yr}]$ at $z = 0$.

The $[\mathrm{OIII}]\lambda 5007$ vs. SFR relation presents a large amount of scatter, regardless of the line luminosity. Overall, the polynomial fit of this relation shows that at a fixed $[\mathrm{OIII}]\lambda 5007$ luminosity the SFR increases towards higher redshifts. However, it is clear from Fig. 5 that $[\mathrm{OIII}]\lambda 5007$ is the less favored SFR indicator from the ones studied here. At around the wavelength of $[\mathrm{OIII}]\lambda 5007$, it is more convenient to use the $\mathrm{H}\beta$ line ($\lambda_{H\beta} = 4861\text{Å}$) as a SFR estimator, since $\mathrm{H}\beta$ is not sensitive to the ionization parameter or metallicity of the ISM.

The $[\mathrm{NII}]\lambda 205\mu\mathrm{m}$ far infrared line is an interesting line to study since it can be detected locally with FIR space based facilities such as Herschel (Zhao et al. 2013), and at high redshifts with submillimetre facilities such as the IRAM Plateau de Bure Interferometer (Decarli et al. 2012) and ALMA (Nagao et al. 2012). Fig. 5 shows that faint $[\mathrm{NII}]\lambda 205\mu\mathrm{m}$ luminosities present a scatter of about an order of magnitude in SFR. However, this scatter is significantly reduced for brighter luminosities. The median SFR for a fixed $[\mathrm{NII}]\lambda 205\mu\mathrm{m}$ luminosity tends to increase for higher redshifts.

The model predictions shown in Fig. 5 are not straightforward to validate. High redshift surveys do not typically attempt to measure the SFR using forbidden lines, since the dependence of the
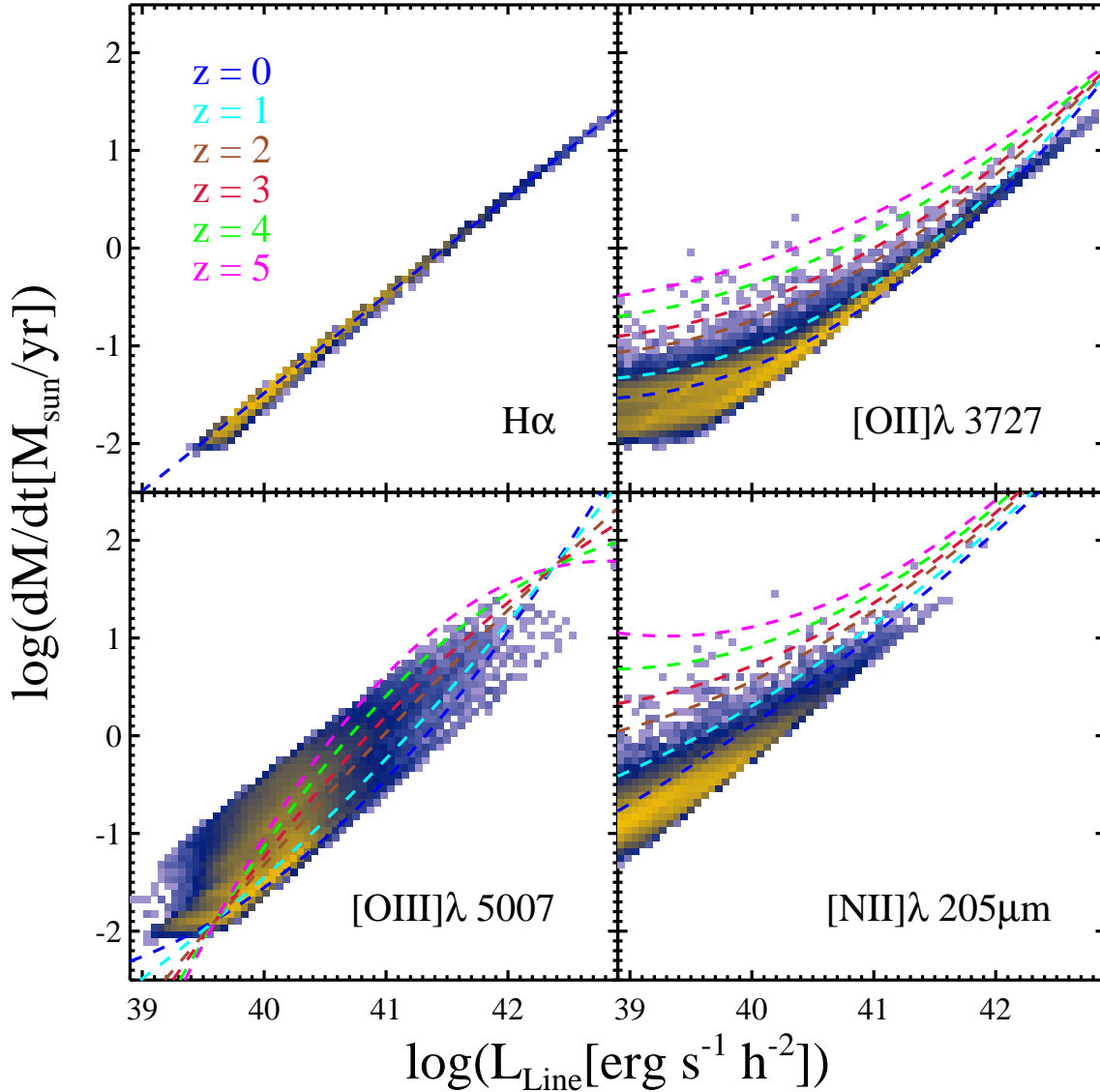
Figure 5. The predicted relation between the star-formation rate and the Hα, [OII]λ3727, [OIII]λ5007 and [NII]λ205μm line luminosities, as shown by the legend. The shaded regions show the density of galaxies in the plot for $z = 0$. The blue, cyan, brown, red, green and magenta dashed lines show fits to this relation for redshifts $z = 0, 1, 2, 3, 4$ and 5, respectively.

line luminosity with the properties of the HII other than the ionizing photon rate is complicated. Even our simple modelling displays a large scatter in the star formation rates that galaxies with a given line luminosity can have. Despite this, the scaling relations using Eq. (7) and Table 1 can provide an approximate value to the star-formation rate of galaxies within an order of magnitude or less.

Hayashi et al. (2013) measured the ratio of Hα to [OII]λ3727 in a sample of line emitters at $z = 1.47$, in an attempt to calibrate [OII]λ3727 as a star-formation rate estimator. We compare our model predictions with the observed line ratios to validate the line luminosities our model predicts. Fig. 6 shows a comparison between the Hayashi et al. (2013) Hα to [OII]λ3727 ratio of star-forming galaxies at $z = 1.47$ and our model predictions. Also, we show Hα/[OII] at $z = 0$ from SDSS.

Our model predicts a steep decrease in the ratio towards brighter [OII]λ3727 luminosities. At $z = 1.47$, Hα is four times brighter than [OII]λ3727 for galaxies with $L_{[OII]} \sim 10^{40}[\mathrm{erg\ s^{-1}\ h^{-2}}]$. At $z = 0$, on the other hand, the Hα luminos-

ity is twice as bright for the same [OII]λ3727 luminosity. Interestingly, galaxies with $L_{[OII]} > 10^{42}[\mathrm{erg\ s^{-1}\ h^{-2}}]$ display a constant ratio, Hα/[OII] ≈ 1.1. This occurs because, as shown in Fig. 4, the majority of galaxies with bright [OII]λ3727 luminosities have a constant ionization parameter value, $q = 10^7[\mathrm{cms^{-1}}]$, making the line ratio constant.

Fig. 6 also shows that our model predicts Hα to [OII]λ3727 line ratios that match those of Hayashi et al. (2013) at $z = 1.47$ remarkably well. Hayashi et al. (2013) observed line ratios are in the range where the line ratios depart from their constant value towards higher ones. In addition, at $z = 0$, we show that our model also predicts line ratios that are consistent with the bulk of the line ratios found in the SDSS spectroscopic sample (Kauffmann et al. 2003). This comparison validates the [OII]λ3727 luminosities that are obtained with our model and their relation with the SFR.

The evolution of the relation between the SFR and the line luminosities shown in Fig. 5 arises due to an evolution of the typical ionization parameter of galaxies with redshift. In our model this
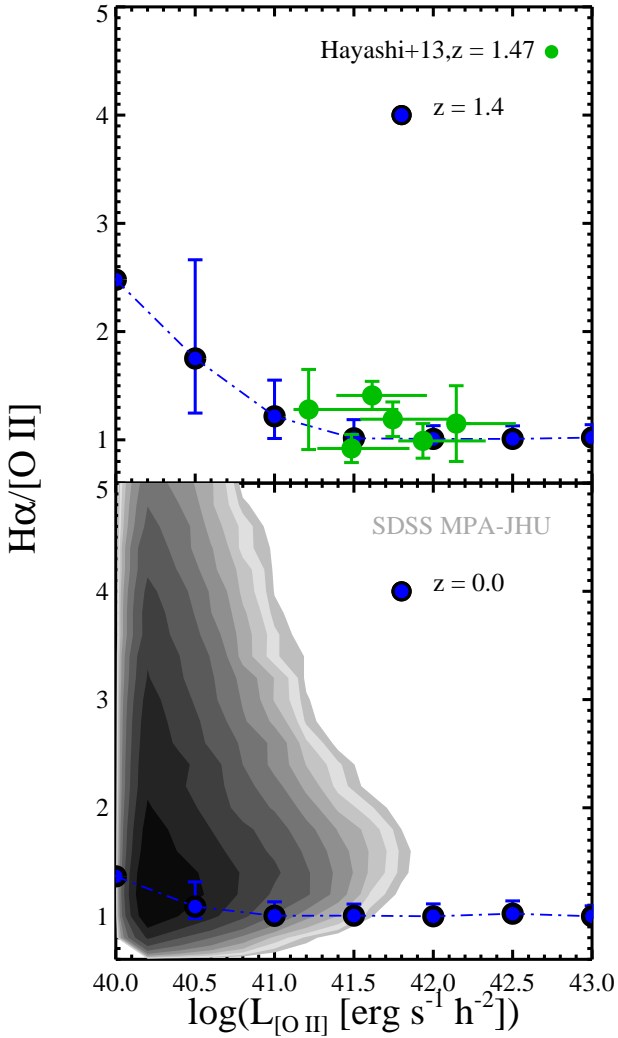
Figure 6. The ratio of Hα to [OII]λ3727 at redshifts $z = 1.47$ (top) and $z = 0$ (bottom). The median of the model predictions are shown by the blue circles. The error bars represent the 10-90 percentile of the distribution at each [OII]λ3727 luminosity bin. Observational data from Hayashi et al. (2013) is shown at $z = 1.47$ (green circles), and from the SDSS (Kauffmann et al. 2003) at $z = 0$. (gray shaded area).
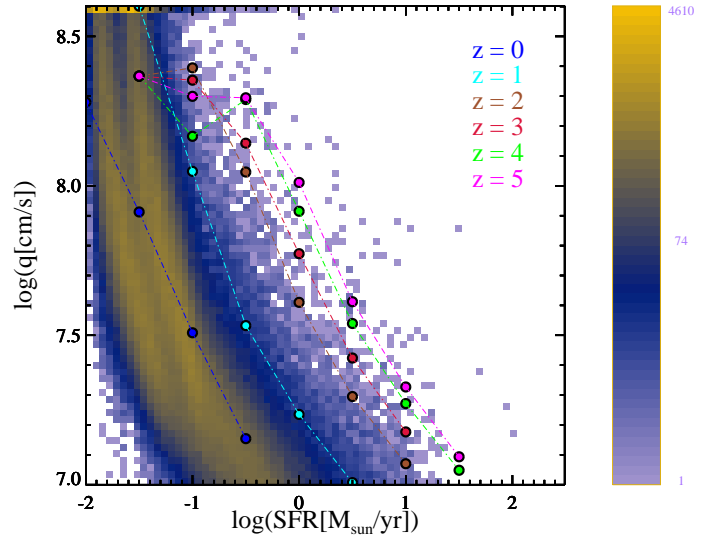

Figure 7. The ionization parameter as a function of star formation rate for redshifts $0 < z < 5$. The squares show the position of galaxies at $z = 0$ for this relation, with bright yellow colours indicating a high concentration of galaxies, and dark blue colors showing less galaxies. Solid circles show the median ionization parameter value at different redshifts.

evolution is driven purely by the cold gas metallicity of galaxies, which is typically lower for high redshift galaxies. Fig. 7 shows the ionization parameter of galaxies between redshifts $0 < z < 5$ as a function of SFR. The median ionization parameter tends to be higher towards higher redshifts for a given SFR. This means that for a given SFR, galaxies have different luminosities depending on the value of the ionization parameter. This creates the evolution of the SFR-line luminosity relation shown in Fig. 5. Also, the scatter in this relation, illustrated at $z = 0$ in Fig. 7 is responsible for the scatter in the SFR versus line luminosity relation.

    The evolution of the ionization parameter with redshift has been suggested as a way to explain the apparent evolution of line ratios in high redshift galaxies (e.g. Brinchmann, Pettini & Charlot 2008; Hainline et al. 2009). By analyzing different line ratios for galaxy samples within the redshift range $z = 0 - 3$, Nakajima & Ouchi (2013) shows that at high redshift star forming galaxies seem to have typical ionization parameter much higher than their low redshift counterparts. A similar conclusion has been reported by Richardson et al. (2013) studying high redshift Lyα emitters. Both

works conclude that is necessary to extend photoionization models to include configurations with ionization parameters greater than $q > 10^9 [\mathrm{cms}^{-1}]$. However, it is important to notice that an evolution of the observed line ratios can arise by other factors than a sole evolution of the ionization parameter, such as the geometry and the electron density of the gas (Kewley et al. 2013a).

4.4 The large scale structure traced by emission lines

Thanks to the increasing development of wide area narrow band surveys of line emitters, it has been possible to map the large scale structure of the Universe at high redshifts using ELGs as tracers (Ouchi et al. 2005; Shioya et al. 2008; Geach et al. 2008; Sobral et al. 2010). However, little is understood in terms of how line emitters trace the dark matter structure, and how the clustering of this galaxy population depends on their physical properties.

    In order to quantify how the line luminosity selection of galaxies trace the underlying dark matter structure, we compute the linear bias, $b = (\xi_{\mathrm{gal}}/\xi_{\mathrm{dm}})^{1/2}$, where ξ_{gal} and ξ_{dm} are the two-point autocorrelation functions of galaxies and dark matter, respectively. Different samples of ELGs are created by splitting them in bins of luminosity with $\Delta \log L = 0.5$ and at different redshifts. Then, the autocorrelation function is computed for each galaxy sample. The dark matter auto-correlation function is computed using a diluted sample of particles from the N-body simulation at different redshifts. The dilution is done in order to compute the correlation function of dark matter efficiently but also so that the error in the bias is dominated by the sample of emission line galaxies. The adopted value for the linear bias is taken by averaging the ratio $\xi_{\mathrm{gal}}/\xi_{\mathrm{dm}}$ over the scales $5 - 15 [\mathrm{Mpc}/h]$, where both correlation functions have roughly the same shape but different normalization.

    The top panel of Fig. 8 shows the linear bias computed for samples selected with different limiting luminosities in the redshift range $0 < z < 5$. Overall, the bias parameter increases towards higher redshifts for all line luminosities, meaning that ELGs are increasingly tracing higher peaks of the matter density field towards high redshifts. ELGs at $z = 0$ have a bias parameter $b \approx 1$, but at
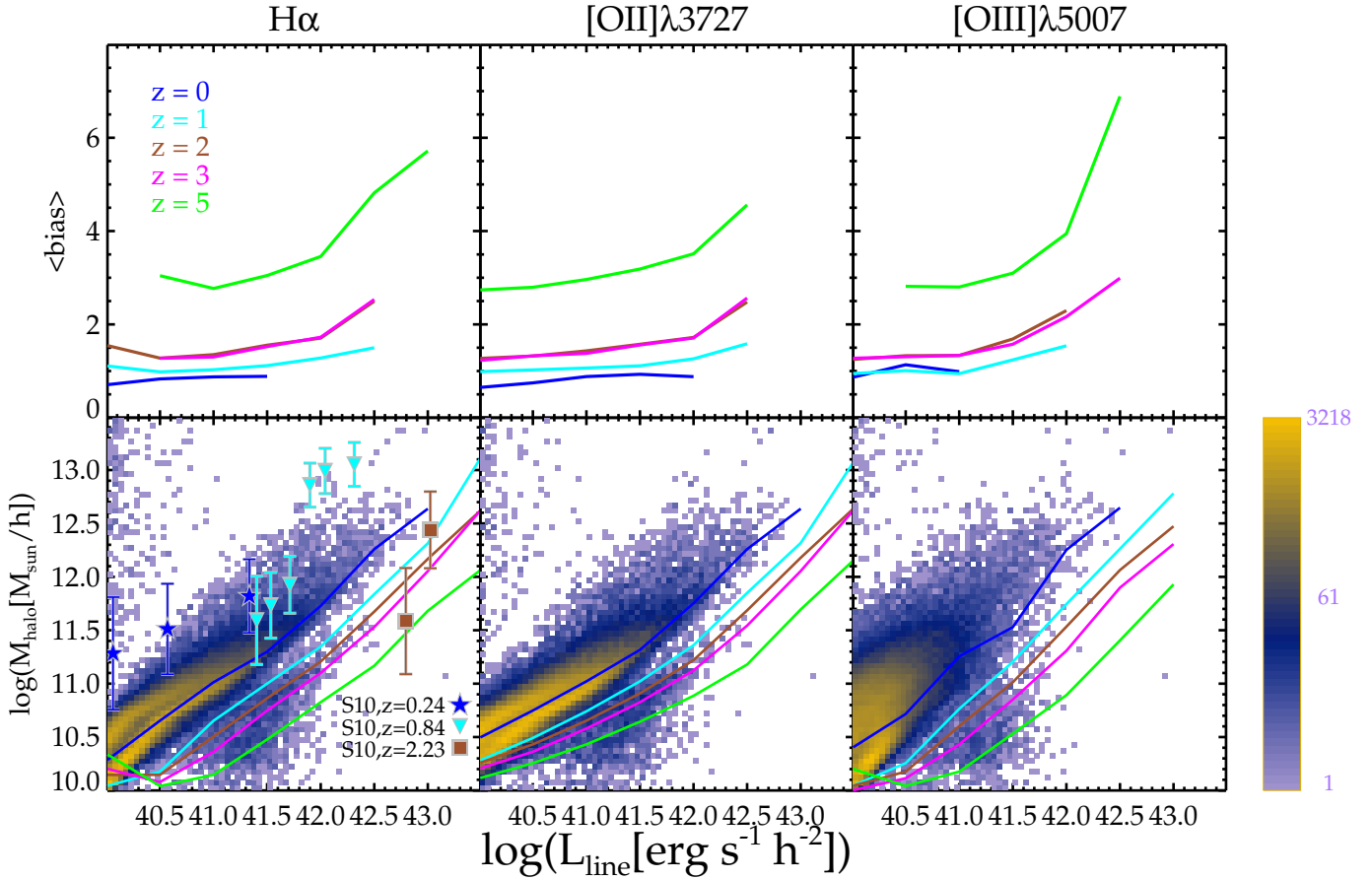
Figure 8. Top panel: Galaxy linear bias for galaxy samples in the redshift range $0 < z < 5$ for Hα (left), [OII]λ3727 (middle) and [OIII]λ5007 (right) emitters. The bias is computed for galaxy catalogues with logarithmic luminosity bins of 0.25. Bottom panel: The dark matter halo mass as a function of line lumiosities, for different redshifts. The colored squares show all the range of halo masses at different luminosities, with brighter yellow colors indicating greater concentrations of galaxies (see the scale on the right). The solid lines show the median halo mass as a function of emission line luminosity for different redshifts. Observational estimates of the minimum dark matter halo mass as a function of Hα luminosity from Sobral et al. (2010) are shown with stars, triangles and squares, for $z = 0.24, 0.84$ and $z = 2.23$, respectively.

$z = 5$ the bias grows rapidly towards $b = 3 - 6$ depending on the line luminosity.

For a given emission line, in general a brighter sample of galaxies is predicted to have a higher bias parameter. The dependence of the bias parameter with the line luminosity also gets steeper towards higher redshifts. At $z = 0$, there is no noticeable dependence between the bias and the line luminosities. At $z = 1$, the bias parameter increases on average by 0.5 between $L_{\text{line}} \sim 10^{40} - 10^{43} [\text{erg s}^{-1} \text{ h}^{-2}]$. At $z = 5$, the bias parameter increases from roughly $b \approx 3$ to $b \approx 6$ depending on the emission line.

The bias parameter predicted for ELGs is overall the same regardless of the emission line chosen. At $z = 5$, however, bright, Hα emitters with $L_{H\alpha} \sim 10^{43} [\text{erg s}^{-1} \text{ h}^{-2}]$ are predicted to have a bias $b \approx 6$. [OIII]λ5007 emitters at $z = 5$ are predicted to have $b \approx 7$ for $L = 10^{43} [\text{erg s}^{-1} \text{ h}^{-2}]$. [OII]$\lambda$3727 emitters, on the other hand, are predicted to reach $b \approx 4.5$ at $z = 5$ for a sample with luminosity $L = 10^{42.5} [\text{erg s}^{-1} \text{ h}^{-2}]$.

At lower redshifts, emission line galaxy samples at $z = 2$ and $z = 3$ are predicted to have the same linear bias overall. In this case, the expected increase in the bias from $z = 2$ to $z = 3$ is balanced by the decrease in the typical halo masses hosting $z = 3$ line emitters, which results in both populations having a remarkably similar bias.

Observational measurements of the linear bias are normally used to infer a typical dark matter halo mass of a sample of galaxies. This is done by making use of a cosmological evolving bias model which makes $b = b(M_{\text{halo}}, z)$ a function of halo mass and redshift (e.g. Mo & White 1996; Moscardini et al. 1998; Sheth, Mo & Tormen 2001; Seljak & Warren 2004).

The bottom panel of Fig. 8 shows the predicted dark matter halo mass of line emitters at different luminosities and redshifts, taken directly from our model. The median dark matter halo mass is found to correlate strongly with the luminosity of the samples. As an illustration, we show the full scatter of this relation at $z = 0$, displaying the scatter around the median value of halo mass that can range up to 1 order of magnitude or more. For a fixed luminosity, the median halo mass is larger for decreasing redshift. Throughout the redshift range $0 < z < 5$, Hα and [OII]λ3727 emitters span the halo mass range $10 < \log(M_{\text{halo}}[\text{h}^{-1}\text{M}_\odot] < 12$ for luminosities between $10^{40} < L_{H\alpha}[\text{erg s}^{-1} \text{ h}^{-2}] < 10^{43}$. [OIII]$\lambda$5007 is predicted to have a steep relation between line luminosity and halo masses. This explains the higher clustering bias of [OIII]λ5007 compared to the other lines. For a given line luminosity, the typical halo mass of [OIII]λ5007 is in general higher than the typical halo mass obtained for the same line luminosity with Hα or [OII]λ3727.

We compare our predictions of the dark matter haloes of emis-

sion line galaxies with available observational data. Sobral et al. (2010) performed a clustering analysis of a sample of $z = 0.84$ Hα emitters and compared it with Hα samples at $z = 0.24$ and $z = 2.23$. Their derived typical halo mass for samples of Hα emitters of a given luminosity are shown in Fig. 8. These were computed by estimating the real-space autocorrelation function of Hα emitters and making use of the Moscardini et al. (1998) evolving bias model to estimate the minimum halo mass of each Hα sample.

For simplicity, we compare our $z = 0$ predictions with the observational sample of Hα emitters at $z = 0.24$, the $z = 0.84$ observational sample with our $z = 1$ predictions, and the $z = 2.23$ observational sample with our predicted $z = 2$ sample. Our model predictions are shown to be marginally consistent with the estimated Hα-halo mass relation at $z = 0.24$, and fairly consistent with the high redshift sample at $z = 2.23$. However, the observationally derived halo masses of Hα emitters at $z = 0.84$ are significantly above the predicted ones with our model. The slope of the Hα-halo mass relation increases drastically between $L_{H\alpha} \sim 10^{41.5} - 10^{42}[\mathrm{erg\ s^{-1}\ h^{-2}}]$ in the Sobral et al. (2010) data, and this is not reproduced in our model.

It is important to notice that the observational samples of Sobral et al. (2010) might be affected by important systematics biasing their results. Firstly, their samples are corrected by dust attenuation by assuming that the extinction of the Hα line is simply $A_{H\alpha} = 1$mag. This is known to be an oversimplification (see, e.g. Wild et al. 2011). The inferred spatial correlation function, used to derive the halo mass of the galaxy sample, relies critically in the redshift distribution of sources, which can also introduce a bias to the results. However, most importantly, the Sobral et al. (2010) samples might be affected by cosmic variance due to the small number of galaxies used to compute the correlation functions. Orsi et al. (2008) show that the effect of cosmic variance can be significantly larger than the statistical uncertainties that can be measured from the data. It is difficult to gauge the effect of cosmic variance in the samples of Sobral et al. (2010) without making a detailed analysis involving the construction of several mock catalogues of the observations. This is beyond the scope of the current work. Details on the procedure to construct mock catalogues of narrow-band surveys can be found in Orsi et al. (2008).

5   PREDICTIONS FOR SUBMILLIMETRE OBSERVATIONS

Searching for the first star forming galaxies is one of the key challenges for the new generation of millimetre and submillimetre facilities. The most appropriate tracers for these high redshift galaxies are FIR emission lines, such as [CII]$\lambda 158\mu$m, [NII]$\lambda 122\mu$m, [NII]$\lambda 205\mu$m and [OIII]$\lambda 88\mu$m. These fine structure, collisional excitation lines provide cooling in regions of the ISM where allowed atomic transitions are not excited (Decarli et al. 2012). Of all these FIR star-forming tracers the [CII]$\lambda 158\mu$m line is the strongest one and it can account for about 0.1-1 per cent of the total FIR flux (Malhotra et al. 2001). Due to the low ionization potential of carbon (11.3eV), [CII]$\lambda 158\mu$m traces the neutral and ionized ISM. Since our model depends on the ionization parameter of hydrogen (with an ionization potential of 13.6eV), our predictions for the [CII]$\lambda 158\mu$m do not account for the neutral regions where [CII]$\lambda 158\mu$m is also produced. Thus, we cannot predict the complete luminosity budget of [CII]$\lambda 158\mu$m. Instead, we turn our attention to other FIR lines that can be targeted with submillimetre facilities. [NII]$\lambda 205\mu$m and [NII]$\lambda 122\mu$m, for instance, can be
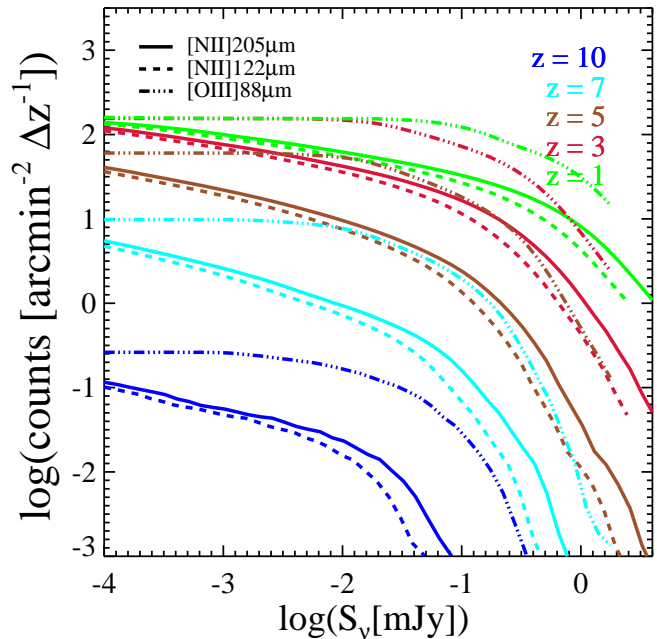

Figure 9. The predicted number of [NII]$\lambda 205\mu$m, [NII]$\lambda 122\mu$m and [OIII]$\lambda 88\mu$m emitters normalized by redshift width as a function of the limiting flux density for galaxies spanning the redshift range $1 < z < 10$.

accounted for in our model, since the ionization potential of ionized nitrogen is 14.6eV, above hydrogen, and so these lines are produced in the ionized medium. The [NII]$\lambda 205\mu$m is expected to become a recurrent target for high redshift objects since it has a nearly identical critical density for collisional excitation in ionized regions than [CII]$\lambda 158\mu$m (Oberst et al. 2006). This makes the line ratio of [NII]$\lambda 205\mu$m to [CII]$\lambda 158\mu$m a sole function of the abundance between the two elements, regardless of the hardness of the ionizing field. Therefore, both the star formation rate and the gas metallicity can be directly measured from observations of these two lines.

The [OIII]$\lambda 88\mu$m line is also expected to be a recurrent target since it is significantly stronger than the ionized nitrogen lines. Recently, by making use of a cosmological hydrodynamical simulation and a photo-ionization model, Inoue et al. (2014) finds that the [OIII]$\lambda 88\mu$m line is the best target to search for $z > 8$ galaxies for submillimetre facilities such as ALMA.

We use our model to compute the number of high-redshift galaxies that could be detected by targeting these FIR lines. Fig. 9 shows the number of [NII]$\lambda 205\mu$m, [NII]$\lambda 122\mu$m and [OIII]$\lambda 88\mu$m emitters predicted to be found in a square arc minute as a function of limiting flux density for different redshifts. An important caveat in this calculation is our assumption of a constant density in the medium, $n_e = 10[\mathrm{cm}^{-3}]$. The ratio [NII]$\lambda 205\mu$m/[NII]$\lambda 122\mu$m, for instance, increases rapidly towards higher values of the density of the gas when $n_e > 10[\mathrm{cm}^{-3}]$ (Oberst et al. 2006; Decarli et al. 2014).

Furthermore, since our model does not compute the line profiles of these lines, in order to obtain the density flux in units of [mJy] we assume for simplicity a top hat profile. The intrinsic line width is chosen to be $v = 50[\mathrm{km/s}]$, consistent with the [NII]$\lambda 205\mu$m width detected in (Oberst et al. 2006). Note that the y-axis is normalized by Δz, meaning that the predicted number of objects at a given redshift will depend on the redshift range covered by the band used to detect the line emission.

Overall, our model predicts that galaxies up to $z = 10$ should

be detectable in blank fields reaching depths that are achievable by the current generation of submillimetre facilities. The beam size of ALMA, for instance, is of the order of a few arc seconds at most, so it would be necessary to perform of the order of hundreds of pointings and reach flux densities of $\sim 10^{-2}[\text{mJy}]$ to detect very high redshift galaxies from a blank field.

Fig. 9 shows that $[\text{OIII}]\lambda 88\mu\text{m}$ is the strongest FIR line from the three shown, with surface number densities up to an order of magnitude larger than the two [NII] lines. At $z = 10$, for instance, $[\text{OIII}]\lambda 88\mu\text{m}$ emitters could be detected by surveying an area of the order of $\sim 10[\text{arcmin}]^2$ with a depth of $S_\nu \sim 10^{-2}[\text{mJy}]$. Since $[\text{NII}]\lambda 205\mu\text{m}$ and $[\text{NII}]\lambda 122\mu\text{m}$ emitters are predicted to be fainter than $[\text{OIII}]\lambda 88\mu\text{m}$, the same flux and area is predicted to detect about the same number of FIR [NII] emitters at $z = 7$. At $z = 10$, on the other hand, these would require a few hundred $[\text{arcmin}]^2$ and a flux density of $\sim 100[\mu\text{Jy}]$ to be detected.

At $z = 5$, FIR lines are predicted to be significantly easier to detect. A square arc minute survey with a flux depth of $\sim 0.01[\text{mJy}]$ should detect tens of $[\text{NII}]\lambda 205\mu\text{m}$ and $[\text{NII}]\lambda 122\mu\text{m}$ emitters, and even a few hundreds of $[\text{OIII}]\lambda 88\mu\text{m}$ emitters per Δz. The number density of FIR line emitters grows by an order of magnitude by $z = 3$ at the same flux depth, and about a factor 2 more by $z = 1$.

Despite the simplifications made, Fig. 9 illustrates that a blind search of FIR lines in SF galaxies down to flux depths and areas achievable with current instruments can successfully result in a significant sample of high redshift objects to perform statistical analysis. Galaxies detected in this way will define a population based only on the limiting flux of the line chosen to trace their SF activity.

6   DISCUSSION

This paper presents the first model for emission line galaxies based on a fully-fledged semi-analytical model of galaxy formation in a hierarchical cosmology scenario. Our approach to model the different line luminosities is to invoke a simple, albeit meaningful, assumption that can lead to a physical interpretation of the predictions. Our model for the luminosities of emission line in star-forming galaxies relies on the critical assumption that the ionization parameter is directly related to the cold gas metallicity via Eq. (5). This assumption is supported by a number of observational and theoretical studies of line ratios of local star-forming galaxies (e.g. Nagao, Maiolino & Marconi 2006; Maier et al. 2006; Dopita et al. 2006b; Groves & Allen 2010; Kewley et al. 2013a, and references therein). However, it is likely that these two quantities are related to each other by a third, more fundamental physical property. For instance, the ionization parameter depends on the gas pressure, which together with the hardness of the ionizing radiation field determine the radii of the HII regions from which the ionization, recombination and collisional excitation processes take place. Hence, HII regions in a typical galaxy can display a distribution of radii, sizes and masses which, in turn, lead to a variety of local ionization parameter values from which the line luminosities are produced (Dopita et al. 2005, 2006a,b). The choice of a global ionization parameter to represent the photoionization process inside a galaxy could hence be an oversimplification, meaning that a more sophisticated model might be required to account for internal structure and dynamics of the ISM of each galaxy.

Despite the above, our simple approach has proven to predict the statistical properties of emission lines, such as the BPT diagram (Fig. 1) and the emission line LF evolution (Figs. 2,3 and 4) in reasonable agreement with observations. Observational estimates

also suggests that the ionization parameter of high redshift galaxies is higher with respect to low redshifts. Models and observations are also suggesting that the line ratios observed in high redshift galaxies seem to imply ionization parameters well above the upper limit of standard grids of photoionization models, $q \sim 10^8[\text{cm/s}]$.

Our model is constrained to lie in this range, so we cannot predict higher ionization parameter values. However, it is encouraging that the model predicts increasingly higher ionization parameters for high redshifts, and that most of the galaxies in the modest SFR regime are predicted to have the highest ionization parameter the version of MAPPINGS-III allows, i.e. $q = 4 \times 10^8[\text{cm/s}]$ (Fig. 7).

There has been recent evidence in the literature of an evolution of the BPT diagram with redshift (e.g. Yeh et al. 2013; Kewley et al. 2013b) from both an observational and theoretical stand point. This evolution is also consistent with the high values inferred for the ionization parameter of high redshift galaxies. In our model, the ionization parameter is constrained to a set of values determined by the gas metallicity, and so therefore there is no evolution in the shape of the BPT diagram at high redshifts, only a redistribution of galaxies along the same sequence.

Our model of galaxy formation also has limitations. The most important one is related to the resolution limit of the dark matter haloes resolved in the N-body simulation used. In this work, the minimum dark matter halo mass is $M_{\min} = 10^{10}[\text{h}^{-1}\text{M}_\odot]$. This limit impacts on semi-analytical models based on N-body merger trees (e.g. Bower et al. 2006), creating an artificial low abundance of faint galaxies with low stellar masses. Only a fraction of these galaxies are hosted by haloes of the minimum halo mass, and the rest should be hosted by haloes with even lower halo mass, which are not resolved by the simulation. This artifact can be seen in the very faint end of the Hα luminosity functions, (Fig. 2), and in the median halo mass of faint line luminosities shown in Fig. 8. Our results and conclusions are based on galaxies with Hα luminosities $L_{\text{H}\alpha} > 10^{40}[\text{erg s}^{-1}\text{ h}^{-2}]$ and stellar masses $M_{\text{stellar}} > 10^9[\text{h}^{-1}\text{M}_\odot]$, which selects galaxies above the halo mass resolution limit, and so should not be affected by this effect.

Another caveat of the model is the evolution of the predicted mass-metallicity relation. The predicted evolution in SAG of the metallicity of the stellar component, tightly related to the cold gas metallicity, is studied in Jiménez et al. (2011) (see their Fig. 6). Overall, the stellar mass and metallicity of galaxies are lower at higher redshifts. However, unlike the apparent evolution of the mass-metallicity relation reported in observations of high redshift galaxies (e.g. Erb et al. 2006; Maiolino et al. 2008; Mannucci et al. 2010) the SAG model shows no evolution in the normalisation of this relation. Galaxy evolution is predicted to increase the stellar component of galaxies and enrich their ISM within the same sequence. This leads to a mass-metallicity relation for local galaxies that is already in place at high redshifts, in disagreement with what the observational estimates show. Since the collisional excitation line strengths are sensitive to the gas-phase metallicity, this could explain the partial disagreement of our model predictions with the observed $[\text{OIII}]\lambda 5007$ LFs at high redshifts.

Despite the lack of evolution in the normalization of the mass-metallicity relation, it is worth pointing out that the observationally inferred values for the gas metallicity, are subject to the biases and limitations imposed by the diagnostic used to infer the metallicities (Kewley & Ellison 2008). This is especially true when applying metallicity diagnostics to high redshift galaxies, where the ISM conditions are likely to be different from what is found in local galaxies (Cullen et al. 2013). The SAG model follows explicitly the chemical enrichment and evolution of 8 different chemical ele-

ments. Therefore, the model computes an absolute value of the gas metallicity which is not straightforward to compare with the values inferred observationally.

An extensive analysis of the mass-metallicity relation, its evolution and the role of the star-formation rate is beyond of the scope of this paper and is discussed in Cora et al. (2014, in preparation).

7 CONCLUSIONS

Throughout this paper we explore the properties and evolution of emission line galaxies within a hierarchical cosmological model. This is the first attempt to model in detail the strong emission lines of galaxies in the optical and FIR range and to study their statistical properties as a galaxy population.

Our method consists in combining the semi-analytical model of galaxy formation `SAG` with the photoionization and shock code `MAPPINGS-III` to predict the emission line luminosities of galaxies. We make the critical assumption of relating the ionization parameter of galaxies with the cold gas metallicity through Eq. (5). We choose the constant values in this relation to achieve a reasonable agreement of the BPT diagnostic and the $[OII]\lambda 3727$ and $[OIII]\lambda 5007$ LFs with the observational data available. We take advantage of the power of semi-analytical models to explore the properties of the ELG population up to redshifts $z = 10$, and present predictions of the detectability of FIR lines that can be targeted with millimeter and submillimetre facilities to explore the high redshift Universe.

We summarize our main findings as follows:

• Overall, our model predicts ELG luminosity functions in close agreement with current observational data. The model predicts an overabundance of Hα emitters at $z \lesssim 0.4$, but is reasonably consistent with the observed LFs in the range $0.9 < z < 2.2$. The luminosity functions of $[OIII]\lambda 5007$ are find to be in partial agreement with observations. The abundance of $[OII]\lambda 3727$ emitters at high redshifts is remarkably close to observed values. There are many reasons that can explain the disagreements between model predictions and observational measurements. First, our model relating the ionization parameter q with the cold gas metallicity Z could be an oversimplification of the complex internal gas dynamics in HII regions of star-forming galaxies. Secondly, the ionization parameter our model computes depends solely on the cold gas metallicity, which implies that if the chemical enrichment histories of galaxies are not realistic in our model then the resulting ionization parameter values we obtain for high redshift galaxies would be incorrect. This would be reflected in the luminosity function of $[OII]\lambda 3727$ and $[OIII]\lambda 5007$. Finally, contamination from AGNs, shock excitation or LINERs might affect the observed luminosity functions in a rather complicated way. Kewley et al. (2013a) shows that the strong line ratios of star-forming galaxies and also AGNs are expected to evolve with redshift, and that diagnostics such as the traditional BPT diagram cannot be applied to discriminate the source of emission lines in the same way that this is done to local galaxies.

• Our model predicts that star-forming galaxies at high redshifts have higher ionization parameters than their counterparts at $z = 0$. A similar conclusion has been suggested in a number of observations (e.g. Brinchmann, Pettini & Charlot 2008; Hainline et al. 2009; Nakajima & Ouchi 2013; Richardson et al. 2013). This is an expected result, since galaxies accumulate metals throughout their star-forming history, and so the bulk of the galaxy population at high redshifts is predicted to have less metal abundances than local galaxies. Since the ionization parameter in our model scales inversely with the metallicity, high redshift galaxies have therefore higher values of the ionization parameter.

• We find that line luminosities can be used to infer the star-formation rate of galaxies, in spite of the scatter of the relation. We fit a polynomial functional form which depends on the emission line luminosity and the redshift of the galaxies. The scaling relations we present are in general accurate to within an order of magnitude for low luminosities and their accuracy improves towards brighter line luminosities. The less favoured emission line to infer the SFR from is found to be $[OIII]\lambda 5007$.

• We find that our model predicts modest values for the clustering of emission line galaxies, roughly consistent with observational estimates of Hα clustering. The bias of emission line galaxies is found to increase towards brighter galaxy samples, especially in high redshift emission line galaxies.$[OIII]\lambda 5007$ emitters present a strong connection between the bias and the line luminosity, and this correlation is found to be weaker in $[OII]\lambda 3727$ and Hα emitters. Overall, ELGs are found to be hosted by dark matter haloes of mass $M_{halo} \lesssim 10^{12} [h^{-1} M_\odot]$.

• We explore the detectability of FIR emission lines with submillimetre observations. $[OIII]\lambda 88\mu m$ is found to be the strongest line, although we do not explore the more common target $[CII]\lambda 158\mu m$. A dedicated survey with ALMA covering several square arc minutes is predicted to find a handful of $[OIII]\lambda 88\mu m$ emitters at $z = 10$ and $[NII]\lambda 205\mu m$ emitters at $z = 7$ if the flux density probes down to a depth of $0.01 [mJy]$.

This is our first paper of a series exploring the properties of strong optical and FIR nebular emission in galaxies. Several improvements can be made to the model to account for more physical processes. For instance, the mid-plane pressure of the ISM could be used to infer an effective ionization parameter. A detailed study of the chemical enrichment of galaxies throughout cosmic time could also prove to be key in validating or ruling out our simple modelling of the ionization parameter.

Regardless of the limitations, this work constitutes the first attempt to explore the properties of emission line galaxies in a cosmological setting. With the advent of ongoing and future large area surveys of emission line galaxies, a detailed understanding of this galaxy population will be regarded as crucial to extract information about the large scale structure of the Universe, and the process of galaxy evolution.

REFERENCES

Abel N. P., Ferland G. J., Shaw G., van Hoof P. A. M., 2005, ApJS, 161, 65

Abramo L. R. et al., 2012, MNRAS, 423, 3251

Baldwin J. A., Phillips M. M., Terlevich R., 1981, PASP, 93, 5

Bergvall N., Zackrisson E., Andersson B.-G., Arnberg D., Masegosa J., Östlin G., 2006, A&A, 448, 513

Blanc G. A. et al., 2011, ApJ, 736, 31

Bower R. G., Benson A. J., Malbon R., Helly J. C., Frenk C. S., Baugh C. M., Cole S., Lacey C. G., 2006, MNRAS, 370, 645

Brinchmann J., Pettini M., Charlot S., 2008, MNRAS, 385, 769

Bruzual G., Charlot S., 2003, MNRAS, 344, 1000

Bunker A. J. et al., 2010, MNRAS, 409, 855

Calzetti D., 2012, ArXiv e-prints

Charlot S., Longhetti M., 2001, MNRAS, 323, 887

Cora S. A., 2006, MNRAS, 368, 1540

Cormier D. et al., 2012, A&A, 548, A20

Cullen F., Cirasuolo M., McLure R. J., Dunlop J. S., 2013, ArXiv e-prints

Dayal P., Ferrara A., Saro A., 2010, MNRAS, 402, 1449

Decarli R. et al., 2014, ArXiv e-prints

—, 2012, ApJ, 752, 2

Dijkstra M., Loeb A., 2009, MNRAS, 400, 1109

Dopita M. A. et al., 2006a, ArXiv Astrophysics e-prints

—, 2006b, ApJ, 647, 244

—, 2005, ApJ, 619, 755

Dopita M. A., Kewley L. J., Heisler C. A., Sutherland R. S., 2000, ApJ, 542, 224

Erb D. K., Shapley A. E., Pettini M., Steidel C. C., Reddy N. A., Adelberger K. L., 2006, ApJ, 644, 813

Ferland G. J., Korista K. T., Verner D. A., Ferguson J. W., Kingdon J. B., Verner E. M., 1998, PASP, 110, 761

Fujita S. S. et al., 2003, ApJ, 586, L115

Gallego J., Zamorano J., Aragon-Salamanca A., Rego M., 1995, ApJ, 455, L1+

Gargiulo I. D. et al., 2014, ArXiv e-prints

Geach J. E., Smail I., Best P. N., Kurk J., Casali M., Ivison R. J., Coppin K., 2008, MNRAS, 388, 1473

Geach J. E., Sobral D., Hickox R. C., Wake D. A., Smail I., Best P. N., Baugh C. M., Stott J. P., 2012, MNRAS, 426, 679

Groves B. A., Allen M. G., 2010, New Astronomy, 15, 614

Groves B. A., Dopita M. A., Sutherland R. S., 2004a, ApJS, 153, 9

—, 2004b, ApJS, 153, 75

Guaita L., Francke H., Gawiser E., Bauer F. E., Hayes M., Östlin G., Padilla N., 2013, A&A, 551, A93

Hainline K. N., Shapley A. E., Kornei K. A., Pettini M., Buckley-Geer E., Allam S. S., Tucker D. L., 2009, ApJ, 701, 52

Hayashi M., Sobral D., Best P. N., Smail I., Kodama T., 2013, MNRAS, 430, 1042

Hayes M., Schaerer D., Östlin G., 2010, A&A, 509, L5+

Hill G. J. et al., 2008, in Astronomical Society of the Pacific Conference Series, Vol. 399, Astronomical Society of the Pacific Conference Series, T. Kodama, T. Yamada, & K. Aoki, ed., pp. 115–+

Hopkins A. M., 2004, ApJ, 615, 209

Inoue A. K., Shimizu I., Tamura Y., Matsuo H., Okamoto T., Yoshida N., 2014, ApJ, 780, L18

Iwata I. et al., 2009, ApJ, 692, 1287

Jarosik N. et al., 2011, ApJS, 192, 14

Jiménez N., Cora S. A., Bassino L. P., Tecce T. E., Smith Castelli A. V., 2011, MNRAS, 417, 785

Kauffmann G. et al., 2003, MNRAS, 341, 33

Kennicutt, Jr. R. C., 1983, ApJ, 272, 54

Kewley L. J., Dopita M. A., Leitherer C., Davé R., Yuan T., Allen M., Groves B., Sutherland R., 2013a, ApJ, 774, 100

Kewley L. J., Dopita M. A., Sutherland R. S., Heisler C. A., Trevena J., 2001, ApJ, 556, 121

Kewley L. J., Ellison S. L., 2008, ApJ, 681, 1183

Kewley L. J., Groves B., Kauffmann G., Heckman T., 2006, MNRAS, 372, 961

Kewley L. J., Maier C., Yabe K., Ohta K., Akiyama M., Dopita M. A., Yuan T., 2013b, ApJ, 774, L10

Kobayashi M. A. R., Totani T., Nagashima M., 2010, ApJ, 708, 1119

Lagos C. d. P., Bayet E., Baugh C. M., Lacey C. G., Bell T. A., Fanidakis N., Geach J. E., 2012, MNRAS, 426, 2142

Lagos C. D. P., Cora S. A., Padilla N. D., 2008, MNRAS, 388, 587

Lara-López M. A. et al., 2010, A&A, 521, L53

Laureijs R. J., Duvet L., Escudero Sanz I., Gondoin P., Lumb D. H., Oosterbroek T., Saavedra Criado G., 2010, in Society of Photo-Optical Instrumentation Engineers (SPIE) Conference Series, Vol. 7731, Society of Photo-Optical Instrumentation Engineers (SPIE) Conference Series

Le Delliou M., Lacey C. G., Baugh C. M., Morris S. L., 2006, MNRAS, 365, 712

Leitherer C., Ferguson H. C., Heckman T. M., Lowenthal J. D., 1995, ApJ, 454, L19+

Leitherer C. et al., 1999, ApJS, 123, 3

Levesque E. M., Kewley L. J., Larson K. L., 2010, AJ, 139, 712

Ly C., Lee J. C., Dale D. A., Momcheva I., Salim S., Staudaher S., Moore C. A., Finn R., 2011, ApJ, 726, 109

Ly C. et al., 2007, ApJ, 657, 738

Madau P., Pozzetti L., Dickinson M., 1998, ApJ, 498, 106

Maier C., Lilly S. J., Carollo C. M., Meisenheimer K., Hippelein H., Stockton A., 2006, ApJ, 639, 858

Maiolino R. et al., 2008, A&A, 488, 463

Malhotra S. et al., 2001, ApJ, 561, 766

Mannucci F., Cresci G., Maiolino R., Marconi A., Gnerucci A., 2010, MNRAS, 408, 2115

Meiksin A. A., 2009, Reviews of Modern Physics, 81, 1405

Mo H. J., White S. D. M., 1996, MNRAS, 282, 347

Moscardini L., Coles P., Lucchin F., Matarrese S., 1998, MNRAS, 299, 95

Nagao T., Maiolino R., De Breuck C., Caselli P., Hatsukade B., Saigo K., 2012, The Messenger, 149, 44

Nagao T., Maiolino R., Marconi A., 2006, A&A, 459, 85

Nakajima K., Ouchi M., 2013, ArXiv e-prints

Nakamura O., Fukugita M., Brinkmann J., Schneider D. P., 2004, AJ, 127, 2511

Oberst T. E. et al., 2006, ApJ, 652, L125

Orsi A., Baugh C. M., Lacey C. G., Cimatti A., Wang Y., Zamorani G., 2010, MNRAS, 405, 1006

Orsi A., Lacey C. G., Baugh C. M., 2012, MNRAS, 425, 87

Orsi A., Lacey C. G., Baugh C. M., Infante L., 2008, MNRAS, 391, 1589

Osterbrock D. E., 1989, Astrophysics of gaseous nebulae and active galactic nuclei, Osterbrock, D. E., ed.

Ouchi M. et al., 2005, ApJ, 620, L1

Panuzzo P., Bressan A., Granato G. L., Silva L., Danese L., 2003, A&A, 409, 99

Pentericci L., Grazian A., Fontana A., Salimbeni S., Santini P., de Santis C., Gallozzi S., Giallongo E., 2007, A&A, 471, 433

Pirzkal N. et al., 2013, ApJ, 772, 48

Raičević M., Theuns T., Lacey C., 2011, MNRAS, 410, 775

Richardson M. L. A., Levesque E. M., McLinden E. M., Malhotra S., Rhoads J. E., Xia L., 2013, ArXiv e-prints

Ruiz A. N. et al., 2013, ArXiv e-prints

Salpeter E. E., 1955, ApJ, 121, 161

Schenker M. A., Stark D. P., Ellis R. S., Robertson B. E., Dunlop J. S., McLure R. J., Kneib J. ., Richard J., 2011, ArXiv e-prints, 11071261

Seljak U., Warren M. S., 2004, MNRAS, 355, 129

Shapley A. E., Steidel C. C., Pettini M., Adelberger K. L., Erb D. K., 2006, ApJ, 651, 688

Sheth R. K., Mo H. J., Tormen G., 2001, MNRAS, 323, 1

Shim H., Chary R.-R., 2013, ApJ, 765, 26

Shioya Y. et al., 2008, ApJS, 175, 128

Siana B. et al., 2007, ApJ, 668, 62

Sobral D., Best P. N., Geach J. E., Smail I., Cirasuolo M., Garn T., Dalton G. B., Kurk J., 2010, MNRAS, 404, 1551

Sobral D., Smail I., Best P. N., Geach J. E., Matsuda Y., Stott J. P., Cirasuolo M., Kurk J., 2013, MNRAS, 428, 1128

Springel V., 2005, MNRAS, 364, 1105

Springel V., White S. D. M., Tormen G., Kauffmann G., 2001, MNRAS, 328, 726

Stark D. P., Ellis R. S., Chiu K., Ouchi M., Bunker A., 2010, MNRAS, 408, 1628

Stasińska G., 2007, ArXiv e-prints

Tecce T. E., Cora S. A., Tissera P. B., Abadi M. G., Lagos C. D. P., 2010, MNRAS, 408, 2008

Tremonti C. A. et al., 2004, ApJ, 613, 898

Troncoso P. et al., 2013, ArXiv e-prints

Wild V., Charlot S., Brinchmann J., Heckman T., Vince O., Pacifici C., Chevallard J., 2011, MNRAS, 417, 1760

Xia L. et al., 2011, AJ, 141, 64

Yeh S. C. C., Matzner C. D., 2012, ApJ, 757, 108

Yeh S. C. C., Verdolini S., Krumholz M. R., Matzner C. D., Tielens A. G. G. M., 2013, ApJ, 769, 11

Yuan T.-T., Kewley L. J., Richard J., 2013, ApJ, 763, 9

Zhao Y. et al., 2013, ApJ, 765, L13